LASER & PHOTONICS REVIEWS
www.lpr-journal.org

Ultraminiature Optical Fiber-Tip 3D-Microprinted Photothermal Interferometric Gas Sensors

Pengcheng Zhao, Kummara Venkata Krishnaiah, Linhao Guo, Taige Li, Hoi Lut Ho, A. Ping Zhang, and Wei Jin**

Optical fiber sensor emerges as a highly promising technology for trace gas detection due to their high sensitivity, remote capability, and immunity to electromagnetic interference. However, the state-or-the-art fiber-optic gas sensors typically use lengthy optical fibers as gas absorption cells or coatings with functional materials to achieve more sensitive gas detection, which poses challenges such as slow response and/or poor selectivity, as well as limitations on their use in confined spaces. Here, an ultraminiature optical fiber-tip photothermal gas sensor via direct 3D micro-printing of a Fabry-Pérot cavity on the end face of a standard single-mode optical fiber is reported. It enables not only direct interaction between light and gas molecules at the fiber output but also remote interrogation through an interferometric read-out scheme. With a low-finesse microcavity of 66 µm in length, a noise equivalent concentration of 160 parts-per-billion acetylene gas is demonstrated with an ultra-fast response time of 0.5 s. Such a small high-performance photothermal gas sensor offers an approach to remotely detecting trace gases for a myriad of applications ranging from in-reactor monitoring to medical diagnosis.

1. Introduction

Laser absorption spectroscopy (LAS) is a widely used optical technique for trace-gas detection, which has many remarkable advantages such as high sensitivity, good selectivity, and rapid response.[1,2] One of the fastest-growing LAS technologies is photothermal interferometry (PTI).[3,4] Gas absorption of a modulated pump beam generates localized heating via the photothermal (PT) effect, which modifies the refractive index (RI) of the gas medium. The RI change is measured by demodulation of the phase change of a probe light propagating through the medium via optical interferometry.

Recently, optical fiber PTI sensors have attracted remarkable attention due to their advantages of small size, high sensitivity, and remote sensing ability, and thus hold great promises for trace-gas detection in remote, space-limited, and harsh environments.[5,6] For instance, Jin et al.[6] demonstrated a near-infrared all-fiber PTI gas sensor using a 10-meter-long hollow-core photonic bandgap fiber (HC-PBF) based Mach-Zehnder interferometer and achieved an extremely low detection limit at parts-per-billion (ppb) level. Yang et al.[7] and Bao et al.[8] presented low-finesse Fabry-Pérot cavity-based PTI gas sensors using a centimeter-long HC-PBF, whose response time is less than 1 min and detection sensitivity is at ppb level. Zhao et al.[9] introduced the evanescent-wave mode-phase-difference PTI technique for trace methane detection using a centimeter-long silica microfiber, whose response time was further shortened to 6 s. Yao et al.[10] and Krzempek et al.[11] demonstrated a hollow-core fiber-based heterodyne interferometry for sensitive PT gas detection in the mid-infrared region, where most gas molecules have stronger intrinsic absorption peaks. However, the effective working lengths of these optical fiber PTI sensors range from centimeters to even meters, which thus limits their wide use in many practical applications, e.g., trace-gas detection in reactors[12,13] or batteries.[14,15]

One of the promising solutions to overcome this limitation is to directly engineer the end face of optical fibers via micro- or nano-fabrication technologies to develop optical fiber-tip PTI sensors. Various kinds of ultrasmall optical fiber-tip sensors, including pressure,[16–20] temperature,[21,22] force,[23,24] and acoustic[25–28] sensors, have been demonstrated for different applications. Optical fiber-tip gas sensors have also been demonstrated by fabricating a Fabry-Pérot (FP) cavity of air cavity-thin film structure on the end face of an optical fiber.[29] After depositing gas-sensitive functional materials, such as palladium or its nanocomposites for hydrogen sensing,[30–33] and graphene oxide (GO)-based nanohybrids or Fe_3O_4-graphene

P. Zhao, K. V. Krishnaiah, L. Guo, T. Li, H. L. Ho, A. P. Zhang, W. Jin
Photonics Research Institute, Department of Electrical and Electronic Engineering
The Hong Kong Polytechnic University
Hong Kong, SAR 999077, China
E-mail: azhang@polyu.edu.hk; eewjin@polyu.edu.hk
P. Zhao, L. Guo, H. L. Ho, W. Jin
Photonics Research Center
The Hong Kong Polytechnic University Shenzhen Research Institute
Shenzhen 518057, China

The ORCID identification number(s) for the author(s) of this article can be found under https://doi.org/10.1002/lpor.202301285

DOI: 10.1002/lpor.202301285

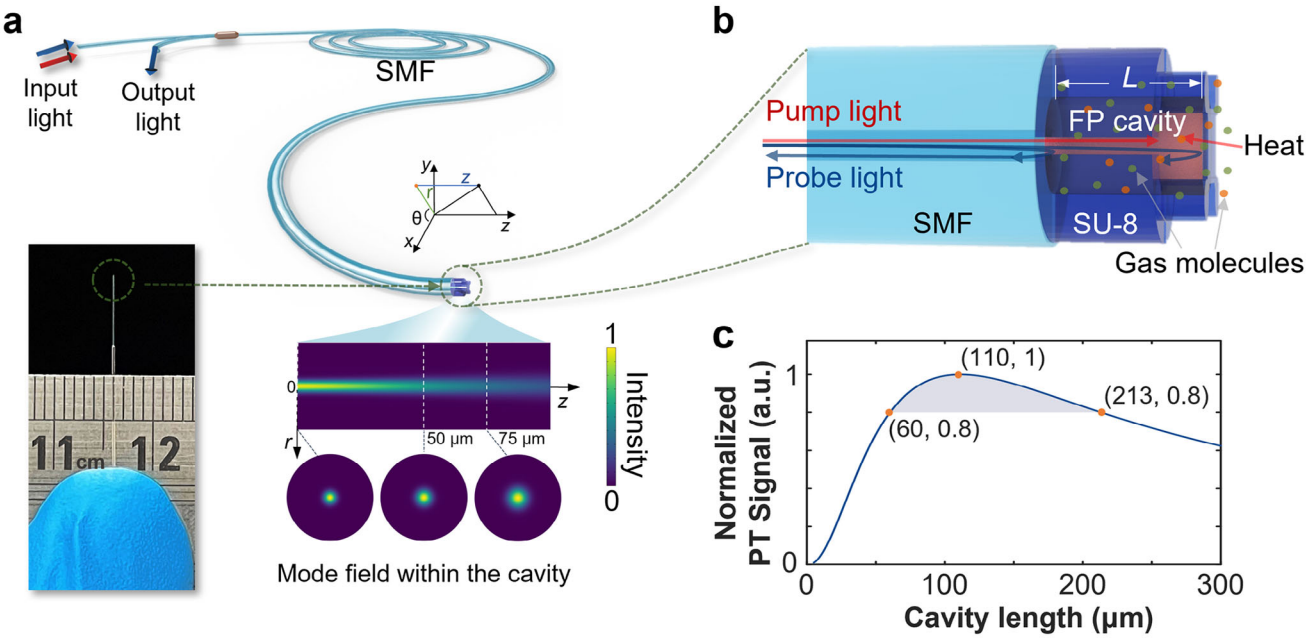

Figure 1. a) Schematic of optical fiber-tip PTI gas microsensor. b) Working principle of Fabry-Pérot cavity-based PT interferometry. The laser absorption by gas molecules induced a change of temperature (hence RI) in the cavity, as marked in red. c) Calculated dependence of PT signal on the cavity length L when the RI modulation frequency is 21 kHz.

composite for ammonia sensing,[34,35] on the thin film, the target gas molecules can be interferometrically detected. However, such functional-material-based gas sensors have shortcomings, such as slow response, limited dynamic range, temperature instability, and cross-sensitivity to other gases.[36]

Here, we report an ultrasmall-size high-performance optical fiber PTI gas sensor based on a fiber-top FP microcavity, for the first time, which is directly 3D microprinted on the end face of a standard single mode fiber (SMF). The microcavity not only provides a micro-chamber for light-gas interaction and modulation of the phase of probe light but also forms a micrometer-scale FP interferometer (FPI) for precise interrogation of PT phase modulation. Based on the theoretical optimization of the cavity length for optimal PT signal, an optical fiber-tip PTI gas sensor with 66 μm-long FP microcavity has been demonstrated to detect acetylene (C_2H_2) at the sub-part-per-million level. Moreover, such an optical fiber-tip PTI sensor exhibited unprecedented response time of less than 0.5 s as well as a large dynamic range and long-term stability in the experiments.

2. Principle and Analysis

2.1. Working Principle of Optical Fiber-Tip PTI Gas Sensors

Figure 1a,b shows the schematic design of the optical fiber-tip PTI microsensor for trace-gas detection. The sensor consists of an SMF for delivery pump and probe lights and collection of probe light signals, and a micrometer-scale FPI that is directly 3D microprinted on the end face of the SMF, as depicted in Figure 1a. The end face of the SMF and the central thin film of the 3D microcavity act as two partially reflective mirrors to form a low-finesse FP micro-interferometer.

The PTI microsensor uses a pump-probe scheme for quantitative detection of gases. Both the pump and probe beams are launched through the SMF into and co-propagate in the cavity, as shown in Figure 1b. To detect C_2H_2 gas, the pump wavelength is selected to be 1532.83 nm, corresponding to the $P(13)$ absorption line of C_2H_2. On the other hand, the probe wavelength is set to ~1550 nm, which resides outside the range of C_2H_2 absorption wavelengths. With the use of SMF, the intensity distribution of both pump and probe beams can be approximated as Gaussian distribution as $I(r,z) = 2P_0/(\pi w_0^2) \cdot \exp[-2r^2/w(z)^2]$,[37] where P_0 is the incident power, r is the radial distance, $w(z) = w_0\sqrt{1+(\lambda z/\pi w_0^2)^2}$ is the mode field radius of the light beam with a wavelength λ at the position z along the direction of propagation in air cavity, and $w_0 = w(0)$ is the mode field radius of the SMF. The mode field distribution of the pump light within the cavity is shown in the inset of Figure 1a.

The pump light is sinusoidally modulated at a frequency f. When the pump beam propagates through the cavity, it is absorbed by C_2H_2 molecules which results in a periodic heating of the gas sample via non-radiative relaxion and consequently modulating the sample's RI. This RI modulation will correspondingly induce a modulation in the phase of the probe beam reflected from the suspended thin film of FP cavity. Under the assumption of weak absorption, the accumulated round-trip PT phase modulation $\Delta\phi$ in the cavity can be written as[6]

$$\Delta\phi = \alpha(\lambda_p)\, C P_p \cdot 2L \cdot \chi(L,f) \tag{1}$$

where α is the gas absorption coefficient at the pump wavelength λ_p, C is the gas concentration, P_p is the pump power, L is the length of the FP cavity, multiplied by 2 to represent the round

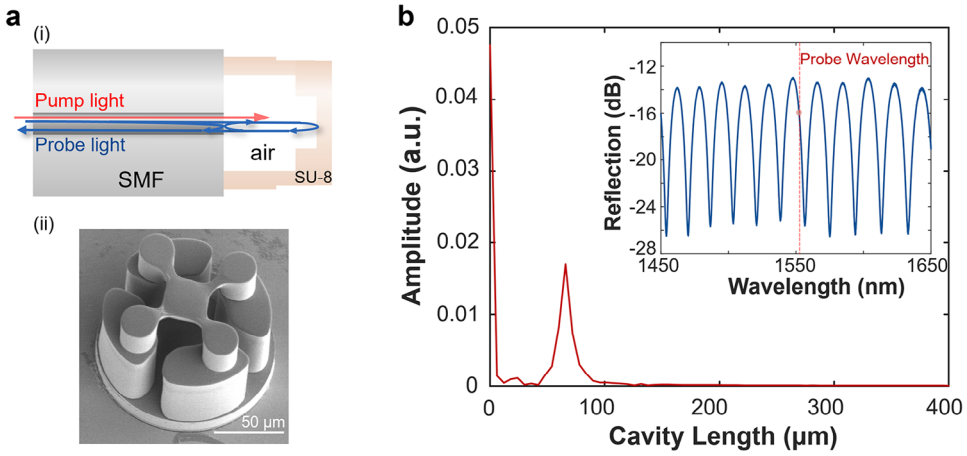

Figure 2. a) Sectional view and SEM image of the 3D microprinted FP cavity. b) The FFT result of the reflection spectrum of the 3D microprinted FP microcavity. The inset in (b) is the corresponding reflection spectrum.

trip of light within the cavity, and χ is the PT phase modulation coefficient. The value of χ depends on L and f due to beam divergence and heat transfer process. The accumulated PT phase modulation can be interrogated by using the 3D microprinted low-finesse FPI, as shown in Figure 1b.

2.2. Cavity Length Optimization for Fabry-Pérot PTI Gas Microsensors

According to Equation (1), in general the accumulated PT phase modulation increases when the cavity length L becomes longer. However, with the increase of cavity length L, $\chi(L,f)$ become a nonlinear function of L and the fringe contrast of such an FPI also diminishes as the intensity of the light reflected from the suspended thin-film of FP cavity decreases owing to beam divergence and mode field mismatch. Consequently, it hampers the efficiency of phase-to-intensity conversion and leads to a degradation of the PT signal. There is a tradeoff between PT phase modulation strength and phase-to-intensity conversion efficiency, which signifies the presence of an optimal cavity length.

Using the numerical model similar to our previous works,[8,38–39] the effect of cavity length L on PT signal in terms of the accumulated PT phase modulation and the fringe contrast, as well as their combined effects are studied, see Note S1 (Supporting Information). Here, the FP cavity is a gas-filled tubular structure, whose two ends are made of silica and SU-8 photoresist, respectively. Figure 1c shows the calculated normalized PT signal as a function of the cavity length L. The optimal L for maximum value of PT signal is ~110 μm. When the cavity length is in the range of 60 to 213 μm, the PT signal can reach or exceed 80% of the maximum value.

3. Experiments and Results

3.1. 3D Microprinted Optical Fiber-Top FP Microcavity

The FP microcavity on the end face of optical fiber is fabricated by using an in-house optical 3D microprinting platform. Epoxy-based SU-8 photoresist is used to fabricate the microcavity because of its good chemical and thermal stability. A two-layer fabrication process was adopted for directly printing the 3D microstructure on the end face of the SMF. The detailed fabrication processes are given in Experimental Section.

Figure 2a shows the sectional view and scanning-electron microscopy (SEM) image of the fabricated FP microcavity. The whole structure is composed of 2 layers. The bottom layer is four surrounded pedestals with a thickness of ~30 μm and height of ~40 μm. The diameter of its central hollow region is ~65 μm. The upper layer consists of four supporting pillars with a diameter of ~25 μm and height of ~26 μm, and a suspended microplate whose central part is with a thickness of ~3 μm. The upper layer stands upon the bottom layer and the central part of the suspended microplate acts as a reflection mirror to form an FP microcavity with the end face of the SMF. The reflection spectrum of the fabricated FP microcavity was measured by using a broadband light source and an optical spectrum analyzer with a wavelength resolution of 0.1 nm, as shown in the inset of Figure 2b. The free spectral range (FSR) and fringe contrast of the resulting interference spectrum around 1550 nm are ~18.2 nm and ~0.89, respectively. The fast Fourier transform (FFT) result of the measured reflection spectrum is shown in Figure 2b, which indicates the cavity length is ~66 μm that is within the optimum length range of 60–213 μm.

3.2. Setup for Testing of Fiber-Tip PTI Gas Sensors

Figure 3 shows the experimental setup for gas detection. The pump laser beam is generated by a 1533 nm distributed feedback (DFB) laser and amplified by an erbium-doped fiber amplifier (EDFA) with a gain of up to 27 dB. The optical filter is used to filter out the amplified spontaneous emission noise of EDFA. Gas concentration measurement is conducted through a combination of wavelength modulation and second harmonic ($2f$) detection techniques. During the experiment, the pump wavelength is slowly scanned across the $P(13)$ absorption line of C_2H_2, while being modulated simultaneously sinusoidally at a higher frequency of

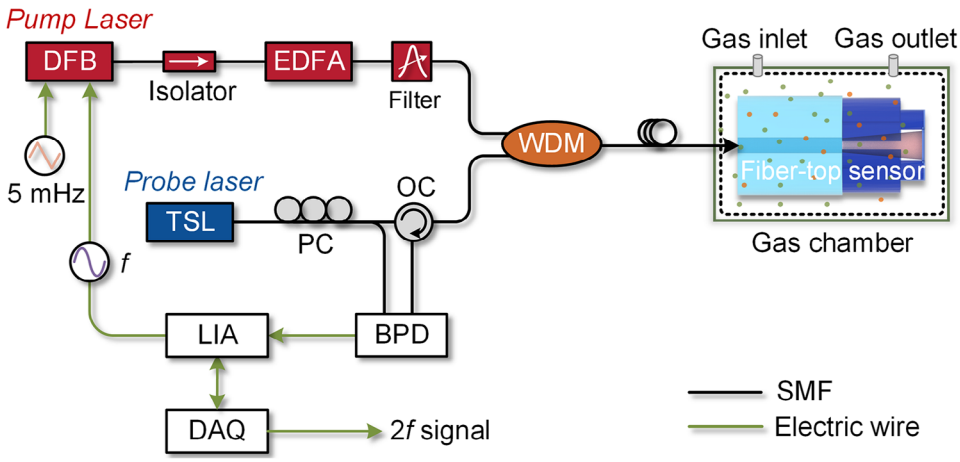

Figure 3. Experimental set-up for testing of optical fiber-tip PTI gas microsensor. DFB, distributed feedback laser; TSL, tunable semiconductor laser; EDFA, erbium-doped fiber amplifier; WDM, wavelength-division multiplexer; PC, polarization controller; OC, optical circulator; BPD, balanced photodetector; LIA, lock-in amplifier; DAQ, data acquisition card.

f = 10.5 kHz to produce periodic RI modulation. Operating at around this frequency, we could achieve high signal-to-noise ratio (SNR) for 2f detection (see Note S1, Supporting Information). The wavelength modulation depth m, defined as the ratio of the amplitude of wavelength modulation $\Delta\nu$ to the linewidth $\Delta\lambda_L$ of the P(13) line of C_2H_2 gas, is set to ~2.2 to maximize the 2f signal. The probe beam is generated by a tunable semiconductor laser (TSL) whose output wavelength can tune across the range of 1500 to 1630 nm. It is combined with the modulated pump via a wavelength-division multiplexer (WDM) before launches into the fiber-tip PTI gas microsensor. The pump power delivered into FP cavity is ~61% of the EDFA output power when taking into account filtering and Fresnel effects. The PTI gas microsensor is placed inside a small-volume gas chamber with two ports for gas exchange.

The probe wavelength is adjusted to a quadrature point of the interference fringe of the PT microsensor around 1550 nm, as illustrated in the inset of Figure 2b. The probe laser beam reflected from optical fiber-tip PTI microsensor passes through an optical circulator and then is detected by a balanced photodetector (BPD) that can reduce probe laser intensity noise. The 2f component from the BPD signal is demodulated by using a lock-in amplifier (LIA). The output from the LIA is recorded by a data acquisition (DAQ) card for post data processing.

3.3. Detection Limit and Response Time

The detection limit of the system is tested by filling N_2-balanced 1001-ppm C_2H_2 into the gas chamber. **Figure 4a** shows the 2f lock-in output signals obtained by scanning the pump wavelength across the P(13) line of C_2H_2 at different input pump power levels. The system noise is measured when the pump wavelength is fixed at the P(13) line center and the gas chamber is filled with pure N_2. The corresponding peak-to-peak value of the 2f signal (i.e., PT signal) and the standard deviation (s.d.) of the noise (i.e., 1σ noise) are shown in Figure 4b, both plotted against the input pump power level. When the pump power delivered to the FP cavity is ~396 mW, the SNR for 1 s lock-in time constant is calculated to be ~1114 gives a noise equivalent concentration (NEC) of 0.90 ppm C_2H_2, corresponding to a noise equivalent absorption (NEA) of ~9.5×10^{-7} cm^{-1}.

To further assess the minimum NEC of the fabricated fiber-tip PTI microsensor for C_2H_2 gas detection, we conducted an Allan-Werle deviation analysis[40,41] based on the noise data over a period of 2 h. The noise data were collected in the same way as above. Figure 4c shows the analysis result as a function of the integration time. When the integration time is less than ~440 s, the NEC decreases with the increase of integration time. When the integration time is 433 s, the NEC goes down to 0.16 ppm C_2H_2, which corresponds to a NEA of ~1.69×10^{-7} cm^{-1}. Besides, the NEC is 0.97 ppm C_2H_2 for 10 s integration time.

The response time of the PTI gas sensor is tested by sequentially filling the gas chamber with pure N_2, 1001 ppm C_2H_2 in N_2, and then pure N_2 at a flow rate of 250 standard cubic centimeters per minute (SCCM) while the pump wavelength is fixed to the center of P(13) absorption line of C_2H_2. Figure 4d shows the real-time recording of the 2f signal, which has been normalized by removing the baseline and scaling them against the maximum value. The response time, specifically the time required for the response reaching 90% (i.e., rise time) and descending to 10% (i.e., fall time) of the maximum 2f signal, is less than 0.5 s.

3.4. Dynamic Range and Long-Term Stability

The dynamic range of the gas sensing system is tested by filling different concentrations of C_2H_2 into the gas chamber at room temperature and atmospheric pressure. **Figure 5a** shows the 2f signals for 100, 200, 500, 751 ppm C_2H_2 when the pump power is 396 mW. Figure 5b presents the peak-to-peak value of the 2f signal as a function of C_2H_2 concentration. From the measured results, the peak-to-peak value and C_2H_2 concentration from 100 ppm to 36.7% can be fitted to a linear relationship, giving a dynamic range of 2.29×10^6 for the lower detection limit of 160 ppb.

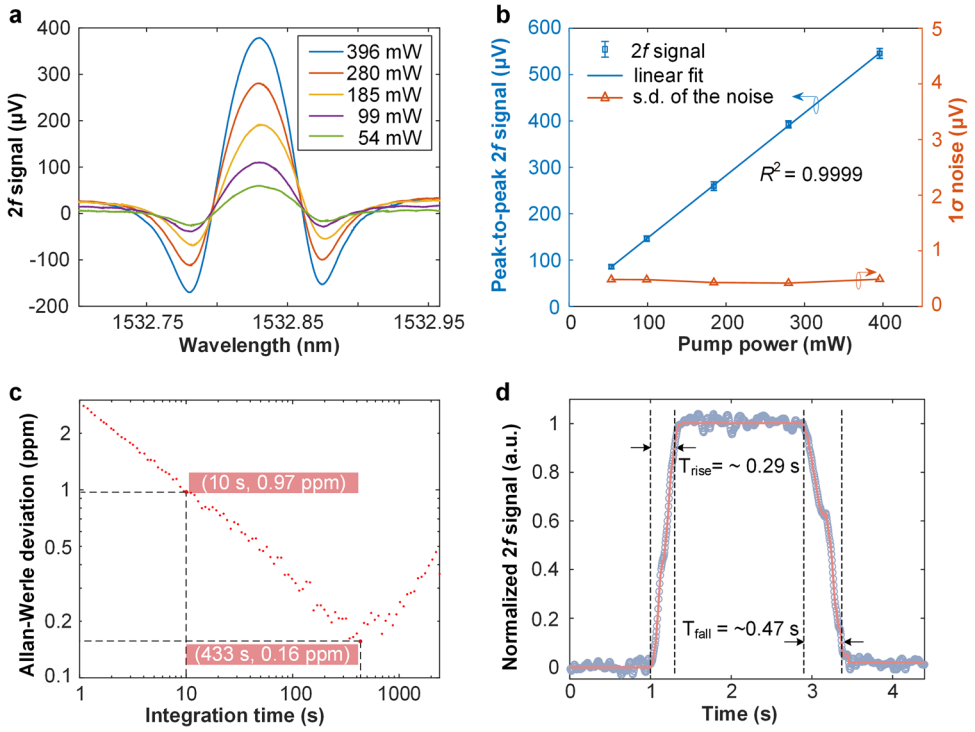

Figure 4. Results of detection limit and response time test. a) Measured 2*f* signals for 1001-ppm C_2H_2 at different input pump power levels. b) Peak-to-peak value of the 2*f* signals and the 1σ noise as a function of input pump power level. Error bars for 2*f* signal show the s. d. of 5 measurements, and the magnitudes of the error bars are scaled up 5-fold for clarity reasons. The mean probe power at the BPD is −9.75 dBm. The lock-in time constant is 1 s and the filter slope is 18 dB Oct^{-1}, corresponding to 0.094 Hz detection bandwidth. **c** Allan-Werle deviation plot based on the noise data over a period of 2 h. d) Response time testing result. At ~1 s, 1001 ppm C_2H_2 gas was loaded into the gas chamber prefilled with N_2 at a flow rate of ~250 SCCM, respectively. At ~3 s, pure N_2 was filled into the gas chamber at the same flow rate. Data in **c-d** are obtained with the detection bandwidth is 3.125 Hz.

The long-term stability of a gas detection system is crucial for practical applications. To assess the system's performance over a long duration, a continuous measurement of 1001-ppm C_2H_2 was conducted in a laboratory environment over 25 h. Figure 5c,d shows the results of this measurement, from which the fluctuation of the peak-to-peak 2*f* signal is ±1.5%.

4. Discussion and Conclusion

According to Equation (1), the PT signal is proportional to the pump power and absorption coefficient. Therefore, an enhanced detection sensitivity could be achieved when a pump source with larger optical power is used. For example, the detection limit could go down to tens of ppb level with 1 W pump power delivered into the cavity. By the use of a mid-infrared laser with stronger absorption strength than the near-infrared as the pump source, the photothermal signal would be significantly enhanced and lower detection limits are expected. Remarkably, the measured response time of the fiber-tip gas sensor is as low as half a second, which can be attributed to the ultrasmall size of the FP microcavity and its side-open structure. It can effectively minimize the time required for gas molecules to reach dynamic equilibrium within the air cavity.

The dynamic range of the system is mainly limited by 2 factors: the effect of wavelength modulation and the nonlinearity of Beer-Lambert Law (see Note S2, Supporting Information). First, for the wavelength modulation and 2*f* detection techniques used in the experiments, the 2*f* coefficient, constituting the PT phase modulation coefficient χ,[42] decreases with the deviation of the wavelength modulation depth $m = \Delta\nu/\Delta\lambda_L$ from its optimal value of ~2.2, which results in a nonlinear relationship between the PT signal and C_2H_2 gas concentration. In the experiments, the amplitude of wavelength modulation $\Delta\nu$ is optimized for relatively low gas concentration (i.e., N_2 balanced 1001 ppm C_2H_2), where the PT signal is proportional to gas concentration. However, the linewidth $\Delta\lambda_L$ expands with the increase of C_2H_2 concentration, resulting in a decrease of m and χ. Consequently, at relatively high gas concentrations, the PT signal exhibits a nonlinear relationship with gas concentration. Second, the amplitude of PT phase modulation $\Delta\varphi$ follows Beer-Lambert's law, being proportional to the gas concentration under low-concentration gas conditions that satisfy the weak absorption limit $\alpha CL \ll 1$, as expressed in Equation (1). The nonlinearity of the Beer-Lambert Law comes into play when gas concentration is continually increased. The combined effect of these two factors is verified by the calculation results, which agree well with the experimental results shown in Figure 5b.

The sensor exhibits remarkable stability and insensitivity to external perturbations due to two factors: 1) the directly 3D microprinted microstructure is highly robust; 2) the short FP cavity with a large FSR of ~18 nm eliminates the requirement for precise control of the probe wavelength at near quadrature point over long durations. A slight systematic fluctuation, shown in Figure 5d, may be caused by the temperature change over one day

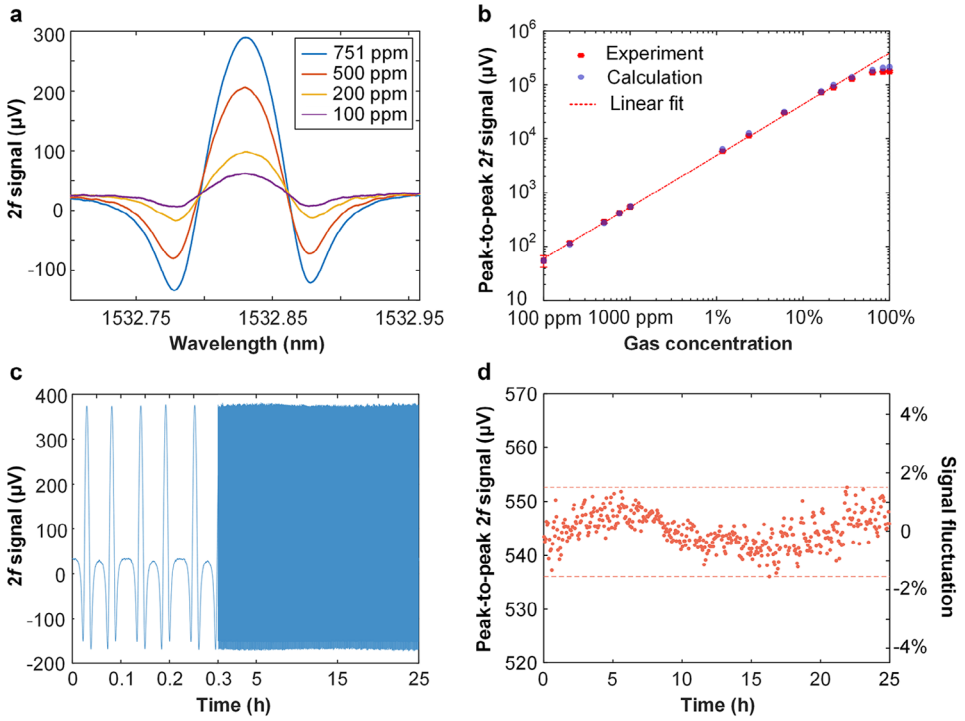

Figure 5. Results of dynamic range and long-term stability test. a) 2*f* signal when pump laser is tuned across the *P*(13) line of C_2H_2 for 100, 200, 500, 751 ppm C_2H_2 at room temperature and atmospheric pressure. b) Peak-to-peak value of the 2*f* signal as a function of gas concentration. The detection bandwidth is 0.094 Hz. Error bars show the s.d. from 5 measurements and their magnitudes are scaled up 10 times for better clarity. c) 2*f* signal over a period of 25 h, and 2*f* signal out of the first 0.3 h is zoomed in for clarify. d) Peak-to-peak 2*f* signal variation over 25 h. Data in (c, d) are obtained with 1001 ppm C_2H_2 in N_2.

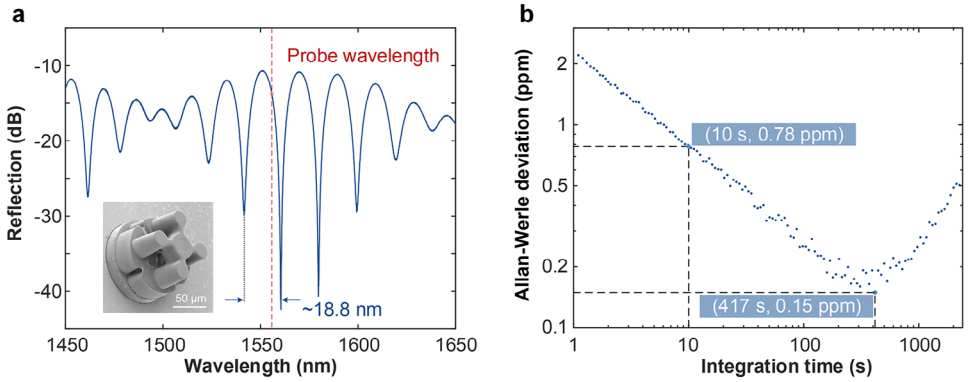

Figure 6. a) Reflection spectrum of the FPI with a slow-changing envelope, The inset in (a) is the SEM image of the corresponding FP microcavity. b) Allan-Werle deviation plots of the FPI based on noise data over a period of 2 h with the detection bandwidth of 3.125 Hz.

since the PT signal is temperature-dependent.[42] The measurement stability can be further enhanced if a precise temperature control of the gas chamber is added to contain the temperature dependence of gas absorption, thermo-optic coefficient, and thermal conductivity of gas mixtures.[42]

It is worth mentioning that the 3D micro-printing technique offers great flexibility in customizing the fiber-top FPI at a micrometer scale. It can tailor not only the length of the FP cavity but also the thickness of the suspended microdisk. **Figure 6a** shows the reflection spectrum of a ~60-μm-long FPI with a relatively thick (i.e., ~6 μm) suspended microdisk. One can see that its spectrum has a clear slow-changing envelope. Such an envelope is commonly employed to enhance the sensitivity and resolution of optical fiber sensor, known as Vernier effect.[43] With this FPI, we also conducted PTI gas sensing and evaluated its performance via Allan-deviation analysis. As shown in Figure 6b, the NEC achieved with 10-s integration time is 0.78 ppm C_2H_2, representing a ~1.4-fold improvement compared to the above-mentioned fiber-tip PTI gas sensor by taking the factor of sensing FPI length into account. The use of the Vernier effect may be explored to further improve the performance of the sensor in the future.

The fiber-tip PTI gas sensor can achieve comparable or better sensitivity, wider dynamic range, and faster response than previously reported miniature laser-based gas sensors, as listed in Table S1 (See Note S3, Supporting Information). Additionally, it exhibits high selectivity and good stability and has the smallest sensor size. The high performance of the proposed sensor renders this technology more suitable for practical applications. It is important to note that in real-world scenarios, the optical fiber should be jacketed and installed in a manner (i.e., bending radius >2 cm) that minimizes bending loss, and a proper packaging of such optical fiber sensors, e.g. using gas permeable membrane, can prevent a direct contact of dusts on the FP cavity, thereby effectively preventing detection performance degradation.

In summary, we have demonstrated a high-performance 3D microprinted fiber-tip FPI photothermal gas sensor for trace-gas detection. The fiber-top FP microcavity not only provides an efficient platform for light-gas interactions and PT phase modulation but also forms an FP microcavity to interferometrically interrogate the PT phase modulation. This unique direct microprinting method renders the fiber-tip microsensor both ultracompact and highly robust. Experimental results have revealed that the fiber-tip PTI gas microsensor has superior performance in the detection of C_2H_2 gas, whose limit of detection can be as low as 160 ppb (when integration time is 433 s), the dynamic range of over 6-order magnitude, ±1.5% instability over a period of 25 h and unprecedented response time of fewer than 0.5 s. Such an ultraminiature PTI gas sensor may open up new possibilities for trace-gas sensing in many space-constrained applications, such as in-reactor or battery monitoring and medical diagnosis, and offer a plug-and-play solution for seamless integration into various scenarios requiring regular inspection.

5. Experimental Section

Fabrication of SU-8 FP Microcavity: EPON SU-8 resin was purchased from HEXION Ltd. Photoinitiator was octoxyphenylphenyliodonium hexafluoroantimonate (OPPI), which was bought from Hampford Research Inc. Inhibitor was tributylamine (TBA) that was purchased from Meryer Chemical Technology Co., Ltd. UV dye 2-(2H-Benzotriazol-2-yl)−4, 6-bis(1-methyl-1-phenylethyl) phenol (Tin 234) was bought from Sigma-Aldrich Ltd. Developer cyclopentanone was purchased from Sigma-Aldrich Ltd. A two-layer printing process was applied to fabricate the SU-8 FP microcavity. The weight ratios of all constituents SU-8 / OPPI / TBA /Tin 234 for the bottom layer and upper layer were 100 / 2 / 0.4 / 0.2 and 100 / 4 / 0.4 / 0.373, respectively. Before the optical exposure process, dip coating was applied to prepare a thin film of SU-8 photoresist. For the bottom layer, 15 wt.% SU-8 solution was used in the dip coating process. Then, the sample was pre-baked at 65 °C for 10 min and 95 °C for 20 min. After UV exposure, a postbake at 65 °C for 30 min was applied. The sample was then washed using a developer. Finally, a hard-bake at 110 °C for 30 min was applied to enhance the mechanical strength of the structure. For the upper layer, similar processes were applied except the concentration of SU-8 solution was changed to 20 wt.%.

Preparation of Gas Samples: Gas mixtures with different concentrations were prepared by mixing calibrated gas samples at ambient temperature and atmospheric pressure with 2 mass flow controllers. For gas concentrations below 1001 ppm, the gas samples were prepared by mixing the calibrated 1001 ppm C_2H_2 with high-purity N_2 with different ratios. For gas concentrations above 1001 ppm, the samples were prepared by mixing high-purity N_2 with high-purity C_2H_2.

Supporting Information

Supporting Information is available from the Wiley Online Library or from the author.

Acknowledgements

The authors acknowledge the financial support from Hong Kong SAR Government GRF Grants (No.: 15221119, 15212220) and the Local Innovative and Research Teams Project of Guangdong Pearl River Talents Program (Grant No.: 2019BT02X105).

Conflict of Interest

The authors declare no conflict of interest.

Author Contributions

P. Z. and K. V. Krishnaiah contributed equally to this work. P.Z. conceived the PTI gas sensors and conducted the testing of the sensors. K.V. K. and A. P. Z. designed the structure of fiber-tip PT microsensors. K.V. K. and T. L. fabricated the microsensors. P.Z. and L. G. performed numerical analysis. H.L.H. assisted in building the testing system and prepared gas mixtures. P.Z., K.V. K., W.J., and A.P.Z. analyzed the results and prepared the manuscript with input from other authors. W.J. and A. P. Z. coordinated the project.

Data Availability Statement

The data that support the findings of this study are available from the corresponding author upon reasonable request.

Keywords

3D microprinting, Fabry-Pérot cavity, fiber-optics, gas sensors, laser spectroscopy

Received: December 5, 2023
Revised: March 15, 2024
Published online: April 25, 2024

[1] B. Fu, C. Zhang, W. Lyu, J. Sun, C. Shang, Y. Cheng, L. Xu, *Appl. Spectrosc. Rev.* **2022**, *57*, 112.
[2] X. Lou, Y. Feng, S. Yang, Y. Dong, *Photon. Res.* **2021**, *9*, 193.
[3] S. Bialkowski, *Photothermal Spectroscopy Methods Chemical Analysis*, **1996**, John Wiley & Sons, New York.
[4] K. Krzempek, *Appl. Sci.* **2019**, *9*, 2826.
[5] W. Jin, H. Bao, P. Zhao, Y. Zhao, Y. Qi, C. Wang, H. L. Ho, *Photonic Sens.* **2021**, *11*, 141.
[6] W. Jin, Y. Cao, F. Yang, H. L. Ho, *Nat. Commun.* **2015**, *6*, 6767.
[7] F. Yang, Y. Tan, W. Jin, Y. Lin, Y. Qi, H. L. Ho, *Opt. Lett.* **2016**, *41*, 3025.
[8] H. Bao, Y. Hong, W. Jin, H. L. Ho, C. Wang, S. Gao, Y. Wang, P. Wang, *Opt. Express* **2020**, *28*, 5423.
[9] P. Zhao, H. L. Ho, S. Fan, W. Jin, *Laser Photonics Rev.* **2023**, 2200972.
[10] C. Yao, S. Gao, Y. Wang, W. Jin, W. Ren, *Sens. Actuators, B* **2021**, *346*, 130528.
[11] K. Krzempek, *Opt. Express* **2021**, *29*, 32568.
[12] S. L. Firebaugh, K. F. Jensen, M. A. Schmidt, *J. Microelectromech. Syst.* **2001**, *10*, 232.

[13] H. Zhang, S. Ju, X. Jin, Y. Yuan, Y. Wu, A. K. Nadda, A. Pugazhendhi, L. Cai, C. Xia, *Renew. Sust. Energ. Rev.* **2022**, *169*, 112915.
[14] T. Cai, P. Valecha, V. Tran, B. Engle, A. Stefanopoulou, J. Siegel, *eTransportation* **2021**, *7*, 100100.
[15] Z. Wang, L. Zhu, J. Liu, J. Wang, W. Yan, *Energy Fuels* **2022**, *36*, 6038.
[16] H. Wei, M. Chen, S. Krishnaswamy, *Appl. Opt.* **2020**, *59*, 2173.
[17] J. Ma, W. Jin, H. L. Ho, J. Y. Dai, *Opt. Lett.* **2012**, *37*, 2493.
[18] Y. Wang, D. N. Wang, C. Wang, T. Hu, *Opt. Express* **2013**, *21*, 14084.
[19] J. Xu, J. He, W. Huang, X. Xu, K. Guo, Z. Zhang, Y. Wang, *Opt. Express* **2018**, *26*, 28178.
[20] X. Wang, J. Xu, Y. Zhu, K. L. Cooper, A. Wang, *Opt. Lett.* **2006**, *31*, 885.
[21] S. Yang, Z. Feng, X. Jia, G. Pickrell, W. Ng, A. Wang, Y. Zhu, *J. Light. Technol.* **2020**, *38*, 1988.
[22] C. Zhu, Y. Zhuang, B. Zhang, R. Muhammad, P. P. Wang, J. Huang, *IEEE Photon. Technol. Lett.* **2019**, *31*, 35.
[23] M. Zou, C. Liao, S. Liu, C. Xiong, C. Zhao, J. Zhao, Z. Gan, Y. Chen, K. Yang, D. Liu, Y. Wang, Y. Wang, *Light: Sci. Appl.* **2021**, *10*, 171.
[24] F. Wang, M. Zou, C. Liao, B. Li, D. Liu, J. Zhou, H. Huang, J. Zhao, C. Liu, P. K. Chu, Y. Wang, *APL Photonics* **2023**, *8*, 096108.
[25] Q. Huang, S. Deng, M. Li, X. Wen, H. Lu, *Opt. Eng.* **2020**, *59*, 064105.
[26] M. A. Cutolo, G. Breglio, *Res. Opt.* **2022**, *6*, 100209.
[27] M. Yao, Y. Zhang, X. Ouyang, A. P. Zhang, H.-Y. Tam, P. K. A. Wai, *Opt. Lett.* **2020**, *45*, 3516.
[28] H. Moradi, P. Parvin, A. Ojaghloo, F. Shahi, *Measurement* **2021**, *172*, 108953.
[29] Y. Xiong, F. Xu, *Adv. Photonics* **2020**, *2*, 064001.
[30] C. Liao, C. Xiong, J. Zhao, M. Zou, Y. Zhao, B. Li, P. Ji, Z. Cai, Z. Gan, Y. Wang, Y. Wang, *Light: Adv. Manuf.* **2022**, *3*, 3.
[31] J. Ma, Y. Zhou, X. Bai, K. Chen, B.-O. Guan, *Nanoscale* **2019**, *11*, 15821.
[32] C. Xiong, J. Zhou, C. Liao, M. Zhu, Y. Wang, S. Liu, C. Li, Y. Zhang, Y. Zhao, Z. Gan, L. Venturelli, S. Kasas, X. Zhang, G. Dietler, Y. Wang, *ACS Appl. Mater. Interfaces* **2020**, *12*, 33163.
[33] J. Zhong, S. Lu, S. Liu, P. Chen, J. Luo, Y. Chen, G. Hong, X. Xu, J. Qu, L. Liu, Y. Wang, Y. Wang, *Lab Chip* **2023**, *23*, 3518.
[34] L. Sansone, V. Malachovska, P. L.a Manna, P. Musto, A. Borriello, G. De Luca, M. Giordano, *Sens. Actuators, B* **2014**, *202*, 523.
[35] D. Pawar, B. V. Bhaskara Rao, S. N. Kale, *Analyst* **2018**, *143*, 1890.
[36] T. Hübert, L. Boon-Brett, G. Black, U. Banach, *Sens. Actuators, B* **2011**, *157*, 329.
[37] C. M. Blanca, C. Saloma, *Appl. Opt.* **1998**, *37*, 8092.
[38] Y. Lin, W. Jin, F. Yang, J. Ma, C. Wang, H. L. Ho, Y. Liu, *Sci. Rep.* **2016**, *6*, 39410.
[39] P. Zhao, Y. Zhao, H. Bao, H. L. Ho, W. Jin, S. Fan, S. Gao, Y. Wang, P. Wang, *Nat. Commun.* **2020**, *11*, 847.
[40] D. W. Allan, *Proc. IEEE* **1966**, *54*, 221.
[41] P. O. Werle, R. Mücke, F. Slemr, *Appl. Phys. B* **1993**, *57*, 131.
[42] P. Zhao, H. L. Ho, W. Jin, S. Fan, S. Gao, Y. Wang, *Opt. Lett.* **2021**, *46*, 2762.
[43] A. D. Gomes, H. Bartelt, O. Frazão, *Laser Photonics Rev.* **2021**, *15*, 2000588.